Testing the UNCOVER paradigm:

Crustal fluid pathways in the

Curnamona Province

Thesis submitted in accordance with the requirements of the University of Adelaide for an Honours Degree in Geophysics

Ben Vincent Kay

October 2017

THE UNIVERSITY of ADELAIDE

TESTING THE UNCOVER PARADIGM: CRUSTAL FLUID PATHWAYS IN THE CURNAMONA PROVINCE

UNCOVER IN THE CURNAMONA PROVINCE WITH MT

ABSTRACT

In July 2017, scale-reduction was undertaken to improve the bandwidth and resolution of the AusLAMP defined Curnamona Conductor (Robertson et al., 2016) by way of a broadband magnetotelluric profile with site spacing of 2 km, extending from the Erudina Domain across the Mudguard and Quinyambie Domains in the Curnamona Province. A fossil fluid pathway has been identified from the lower mid crustal conductor to the near surface situated near a topographic basement high. The upper crustal conductor has been further delineated beneath the Quinyambie Domain to within 5 km of the surface situated alongside a major crustal feature.

KEYWORDS

Magnetotellurics, crustal fluid, UNCOVER, Curnamona Conductor, scale-reduction

TABLE OF CONTENTS

LIST OF FIGURES AND TABLES

INTRODUCTION

A significant challenge for the global mineral exploration industry is to identify the deep signature of world-class mineral deposits and the conceptual understanding of terrane scale fertility under cover at which mineral systems operate. By approaching this from a mineral system viewpoint, with their deep sources and fluxes that are magnitudes higher on a spatial scale (McCuaig & Hronsky, 2014), and through scale reduction by narrowing the exploration space from terrane to camp will improve the predictive ability for mineral exploration under cover in Australia.

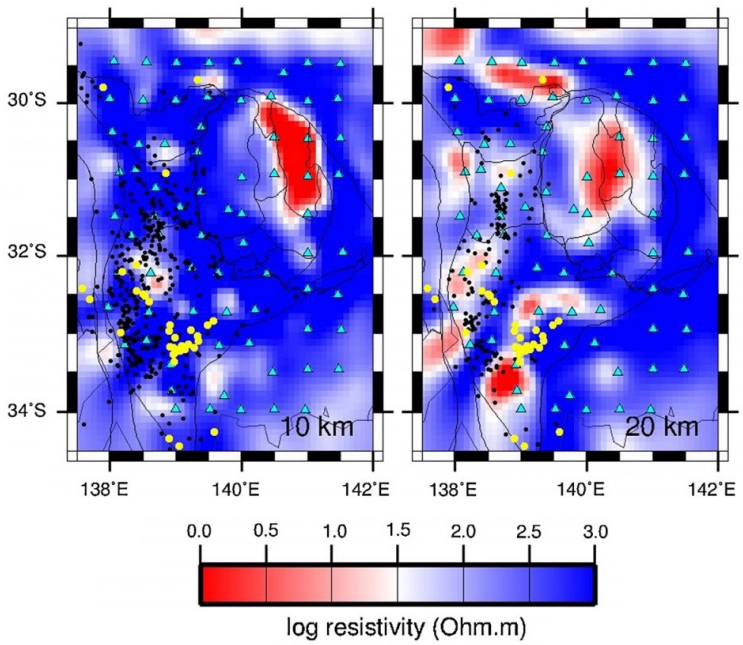

Figure 1: Resistivity depth slices from 3D inversion of AusLAMP data at 10 km and 20 km from (K. Robertson, Heinson, & Thiel, 2016)**. Blue triangles are AusLAMP MT stations, yellow circles are discovered diamonds and black circles are earthquake hypocentres.**

The Curnamona Province is a near circular province of Paleoproterozoic to Mesoproterozoic rocks in north east South Australia and western New South Wales that is predominantly covered by the younger sediments of the Arrowie basin. Robertson et al., (2016) showed significant resistivity heterogeneity in the mid to lower crust in the Curnamona Province from the Australian Lithospheric Architecture Magnetotelluric Project (AusLAMP) deployments of long period (1 – 10,000 seconds) magnetotelluric (MT) stations spaced approximately 50 km apart (Figure 1). These resistivities of the mid to lower crust in the Curnamona Province are more than two orders of magnitude lower than surrounding crustal units. The lowest resistivity is observed at the brittle-ductile boundary at about 10 km (Thiel, Soeffky, Krieger, Peacock, & Heinson, 2016) which is consistent with crustal permeability models (Connolly & Podladchikov, 2004) where fluids have accumulated below the brittle-ductile boundary, until overpressure results in hydro-fracturing of the brittle crust above.

The AusLAMP array with site spacing of 50 km is designed for terrane investigation, the large site spacing lacks resolution and bandwidth to define potential fluid pathways from the upper middle crustal fluids to the surface. Hence, the goal of this research is to increase the current understanding of potential connections between the mid to lower crustal Curnamona Conductor identified by Robertson et al., (2016), as shown in Figure 1, and the surface through scale reduction using broadband MT instruments.

Geological Background

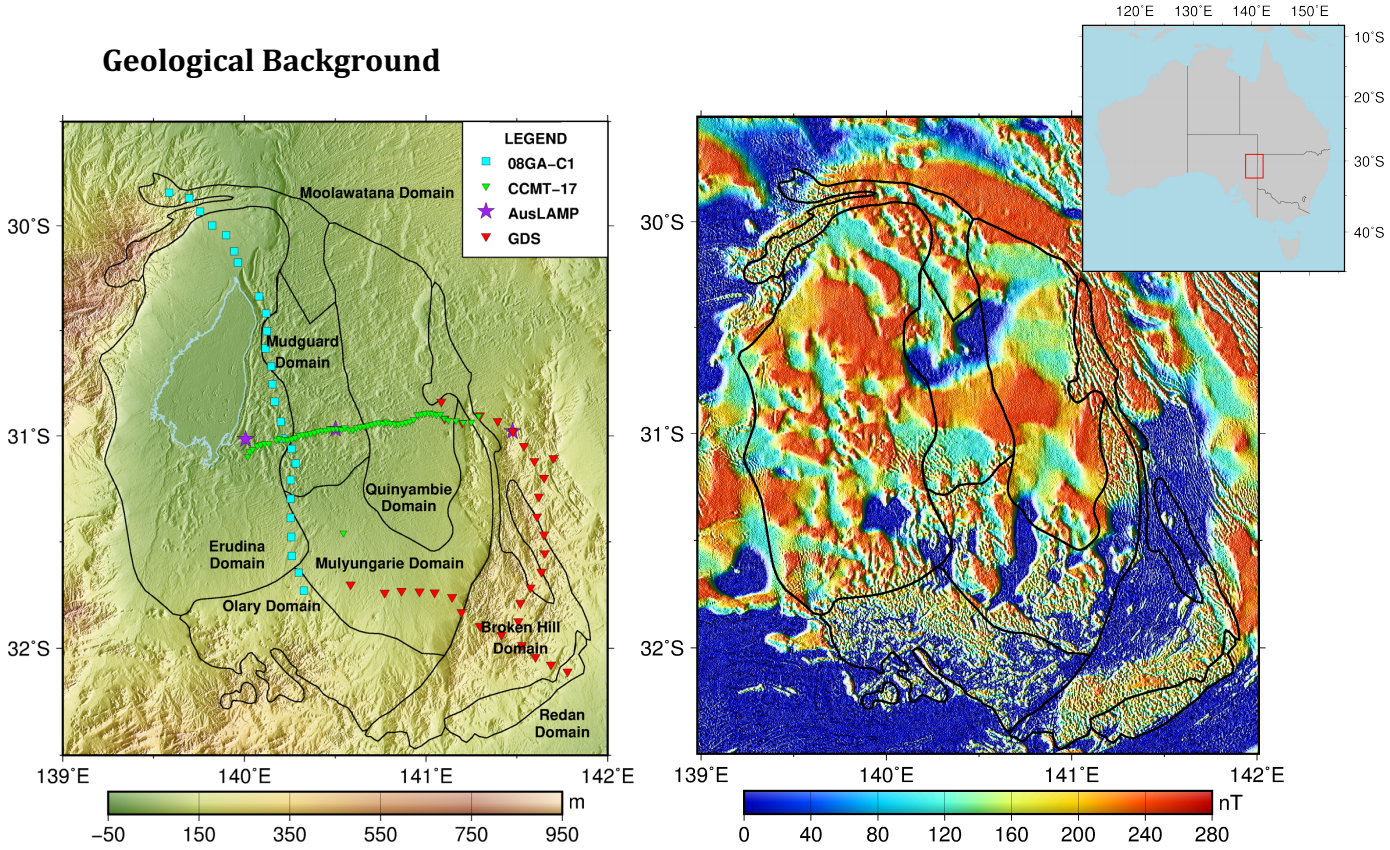

Figure 2: left: Topography map of the Curnamona Province showing clearly visible outcrop in the Olary, Broken Hill and Moolawatana Domains. Right: Total Magnetic Intensity (TMI) map of the Curnamona Province showing location of Geological Domains. Insert map showing location of map extent in Australia. Black boundaries are the Geological Domains modified from (Conor & Preiss, 2008), blue boundary is Lake Frome. Green triangles showing CCMT-17 transect which cuts across strike of the Erudina, Mudguard and Quinyambie Domains. Other symbols showing different EM studies conducted in the Curnamona Province.

The Curnamona Province straddles the border between north eastern South Australia and western New South Wales with an ovoid shape made up of continental crust from the Proterozoic to Mesoproterozoic that was delineated from its distinct magnetic signature (R. Robertson, Preiss, Crooks, Hill, & Sheard, 1998) as shown in Figure 2. The Curnamona Province is separated from the Archean-Mesoproterozoic Gawler Craton to the east by the Neoproterozoic Flinders Ranges (Preiss, 2000). Outcrop in the province, easily identifiable from the topography in Figure 2, is mostly restricted to the Mount Painter region in the north west, consisting of Mesoproterozoic basement rocks from the Neoproterozoic, and the Broken Hill and Olary domains towards the south, consisting mostly of the Paleoproterozoic Lower Willyama

Supergroup (Conor & Preiss, 2008). Much of the province is concealed by younger sedimentary cover (R. Robertson et al., 1998) of Neoproterozoic to Holocene age (Fricke, Preiss, & Neumann, 2010). A- and S-type magmatism has occurred in three main phases between ~1715 and 1580 Ma throughout the Curnamona Province (Conor & Preiss, 2008). The Curnamona Province has experienced two major orogenic events, namely the Mesoproterozoic Olarian Orogeny (~1600 Ma) and the Paleozoic (~500 Ma) Delamerian Orogeny, both of which have resulted in regional metamorphism and deformation (Page & Laing, 1992).

Connor & Preiss (2008) divided the Curnamona Province into seven different domains based on age, facies, magmatism and metamorphism. The domains of interest in this study are the Mudguard, Erudina and Quinyambie Domains from which the MT transect CCMT-17 shown in Figure 2 cuts across strike. The Mudguard Domain contains a relatively undeformed sheet of Mesoproterozoic A-type bimodal Benagerie volcanics of ~1590 Ma inferred from geophysics and drillholes (Preiss et al., 2004). The Benagerie volcanics unconformably overlie the Upper Willyama Supergroup under relatively thin cover situated on the Benagerie Ridge, which itself is flanked by the younger rift related Yalkalpo and Moorowie sub basins to the east and west, respectively (Fricke et al., 2010).

The Yalkalpo and Moorowie sub-basins formed from reversal of crustal stresses in the early Cambrian during the Delamerian Orogeny, that resulted in northwest to southeast rifting along predominantly northeast to southwest faults into the Upper Willyama Supergroup (Roach, Jaireth, & Costelloe, 2014). From this reversal, numerous large scale crustal faults developed, or reactivated, with the Mundi Mundi and Kantappa Faults controlling the eastern edge of the Moorowie sub-basin and the Paralana,

Wooltana, Four Mile and Poontana Faults controlling the western edge of the Yalkalpo sub-basin. Little is known about the Yalkalpo and Moorowie sub-basins due to Cretaceous Frome Embayment and Cenezoic Callabonna sub-basin sedimentary cover and sparse drillings. Roach (2012) mentions that the Moorowie sub-basin predominately consists of deep water marine sediments > 5 km deep while the Yalkapa sub-basin primarily consists of shallow marine sediments approximately 2 km deep.

The A-type granites of the Benagerie Ridge are potentially correlative with the Hiltaba Suite volcanics of the Gawler Craton that are considered equivalent of age at ~1590 (Fricke et al., 2010). Kositcin (2010) describes how the Gawler Range Volcanics can also be considered equivalent to the A-type felsic rocks from the Benagerie Ridge. This is of interest to mineral explorers, as the Hiltaba Suite hosts numerous IOCG deposits. This makes the Curnamona Province highly prospective, but most of the central Curnamona is covered in sediments and can be classified as greenfields territory.

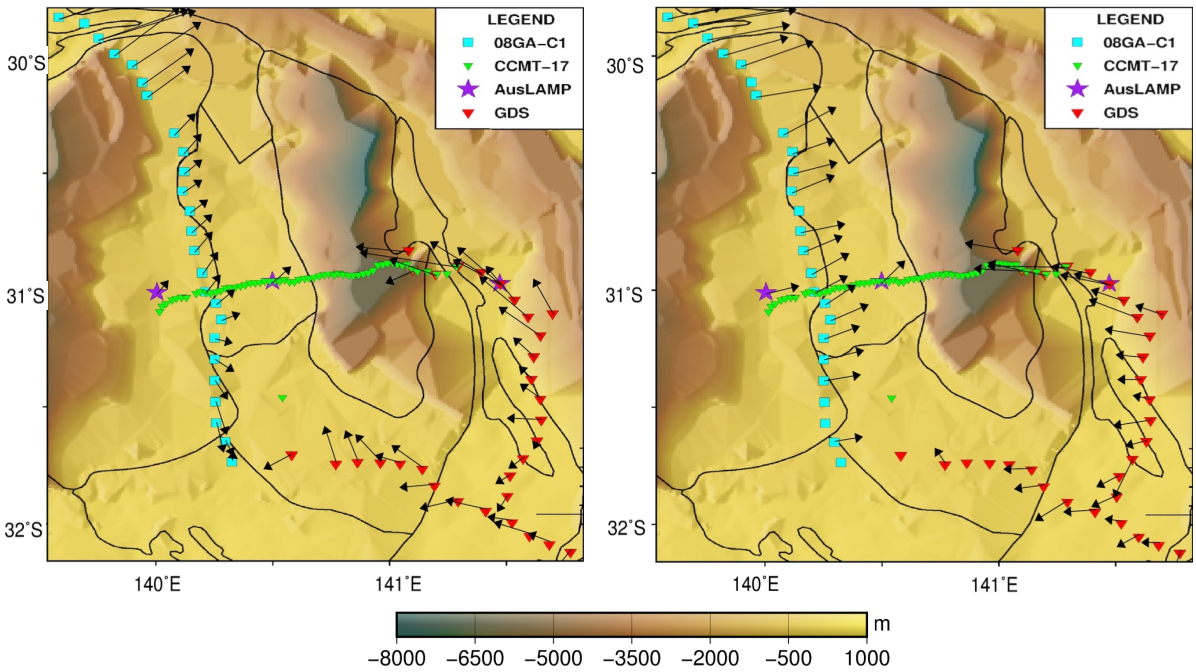

Figure 3: Left: The real part of the induction arrows for 0.005 Hz (200 s). Right: The real part of the induction arrows for 0.001 Hz (1000 s). Both are overlain on depth to Proterozoic basement from OzSEEBASE. The arrows are in the Parkinson convention and show a regional trend towards the Quinyambie Domain.

Magnetotelluric Theory

The magnetotelluric method was first introduced by Tikhonov (1950) and further refined by Cagniard (1953) in greater detail. Maxwell's equations are fundamental for the theory of MT, in which they describe the behaviour of both magnetic and electric fields and their interactions at varying frequencies.

$$\nabla \cdot E = \rho_f \tag{1.1}$$

$$\nabla \cdot B = 0 \tag{1.2}$$

$$\nabla \times E = -\left(\frac{\partial B}{\partial t}\right) \tag{1.3}$$

$$\nabla \times H = J + \left(\frac{\partial D}{\partial t}\right) \tag{1.4}$$

Where equation 1.1 states the divergence of the electric flux density, E, is equal to the electric charge density, ρ_f, inside a closed surface. Equation 1.2 shows that since there are no magnetic charges, the divergence of the magnetic flux density, B, will always be zero through a closed surface. Equation 1.3, Faraday's Law, shows that an electric current can induce a magnetic field and that a changing magnetic field in a closed loop will produce an electric current. Equation 1.4, Ampere's Law, states how a flowing electric current, J, induces a magnetic field that encircles the current

The MT method is a passive (natural-source) geophysical imaging technique which images the electrical resistivity (or its inverse, conductivity) of Earth's subsurface to depths of up to 600 km (Simpson & Bahr, 2005)(Chave & Jones, 2012). This is done by measuring Earth's time-varying magnetic, ***B***, and electric, ***E***, fields in two orthogonal directions, ***x*** and ***y*** (north-south and east-west, respectively), at the surface, with the optional ***z*** measurement of the magnetic field for long period soundings. After

Fourier transforming, observations are made over a wide range of periods, $\boldsymbol{T}$, from between 10^{-3} – 10^{4} s (or between frequencies of 10^{3} – 10^{-4} Hz). The dead band, at frequencies of 0.5 – 5 Hz, results in a low signal-to-noise ratio in the observed data from the low amplitude of the natural source signal (Chave & Jones, 2012). The MT measurements presented throughout this paper have a period bandwidth of 10^{-3} - 10^{3} s (or between frequencies of 10^{3} and 10^{-3} Hz).

The impedance tensor $\boldsymbol{Z}$ represents how the measured electric and magnetic fields in the frequency domain have been altered by the Earth's resistivity structure, is defined as:

$$\begin{pmatrix} E_x \\ E_y \end{pmatrix} = \begin{pmatrix} Z_{xx} & Z_{yx} \\ Z_{yx} & Z_{yy} \end{pmatrix} \begin{pmatrix} H_x \\ H_y \end{pmatrix} \tag{2.1}$$

From Maxwell's equations, we know that the electric field and magnetic fields are orthogonal; from such orthogonal relation, due to the inherent nature of the plane wave source waves, the measured fields can be decoupled into separate components (Simpson & Bahr, 2005). In this paper, the north-south polarisation of the electric field refers to Z_{XY}, while the east-west polarisation for the magnetic field refers to Z_{YX}. For a 1D Earth:

$$Z_{xy} = -Z_{yx} = Z, \quad Z_{xx} = Z_{yy} = 0 \tag{2.2}$$

While for a 2D Earth, the impedance tensor may be rotated parallel to geoelectric strike, such that:

$$z = \begin{pmatrix} 0 & Z_{yx} \\ Z_{yx} & 0 \end{pmatrix}, \; Z_{yx} \neq Z_{xy} \tag{2.3}$$

This decoupling of the Z_{xy} and Z_{yx} polarisations from each other makes them independent; in this coordinate frame, the impedance tensor elements represent the transverse electric (TE) and transverse magnetic (TM) modes, respectively.

The apparent resistivity ρ_a can be calculated from the magnitude of the impedance component, which is interpreted as being an equivalent to the uniform half-space down to the signals penetration depth. Thus, higher frequencies will result in greater resolution at the near surface but experience less depth penetration while lower frequencies will have lower resolution but reach greater depths. This is given by:

$$\rho_{aij} = \frac{|Z_{ij}|^2}{\mu_o \omega} \tag{2.4}$$

Where, the angular frequency, $\omega = 2\pi f$, and the magnetic permeability, $\mu_o = 4\pi \times 10^{-7}\ H\ m^{-1}$. In addition to using the magnitude of the impedance, the phase of the impedance can be used to calculate the shift between the magnetic and electric fields. This is given by:

$$\phi_{ij} = tan^{-1}\left(\frac{\Im(Z_{ij})}{\Re(Z_{ij})}\right) \quad i,j\,\epsilon(x,y) \tag{2.5}$$

Jones (1988) showed how the regional resistivity can be mapped without effects such as static shift of the MT impedance from using induction arrows, which show more sensitivities to lateral variations of resistivity. By using the Parkinson convention, real arrows point towards areas of higher conductivity from resistive areas.

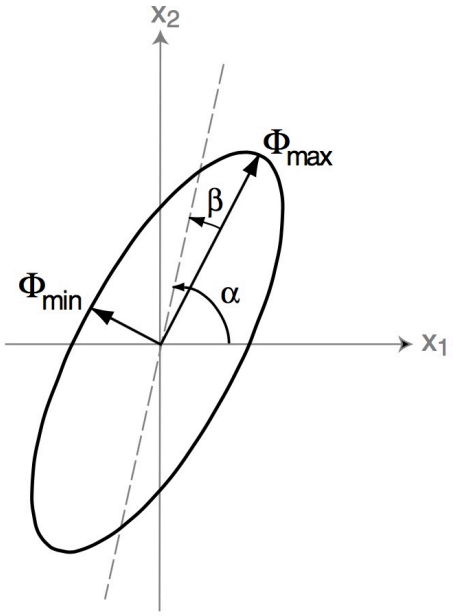

Figure 4: The Phase Tensor shown graphically as an ellipse. The axes of the ellipse are represented by the maximum and minimum phase (Φ_{max} and Φ_{min}). The rotation from the reference axis (dashed line) is represented by the skew (β) and represents 3D structure (non-symmetric). Figure from (Caldwell, Bibby, & Brown, 2004).

Caldwell et al., (2004) showed that from using a graphical representation of the invariant of the impedance tensor it is possible to visualise the phase tensor without distortion effects (Figure 4). The overall shape and size of the phase tensor ellipse indicate the strength and direction of induction (Caldwell et al., 2004).

The frequency of the signal as well as the bulk resistivity of the subsurface determines the penetration depth of the signal and is given by the skin depth equation.

$$\delta \approx 500\sqrt{\rho_a T} \tag{2.6}$$

Where δ is the skin depth in meters, ρ_a is the apparent resistivity and T is the given period.

SURVEY

An MT survey, CCMT-17, was conducted along a 120 km east-west transect across the central Curnamona Province in two phases (Figure 1). The first survey consisted of 48 broadband stations at intervals of 2 km collected from the 6th – 15th July 2017 in South Australia with a remote-reference station located 50 km south of the transect. The aim of the remote reference is to reduce the signal-to-noise ratio and improve the signal in the dead band by utilising an adjacent site that were recorded simultaneously (Gamble, Goubau, & Clarke, 1979). The second survey consisted of 10 broadband stations spaced at intervals from 2 - 4 km in New South Wales collected from the 25th – 27th July 2017, with each site remotely referenced to an adjacent site. Four components (B*x*, B*y*, E*x*, E*y*) were recorded for approximately 45 hours for each station, with a sample rate of 1000 Hz using the GSSA-AuScope LEMI-423 wide band MT instruments.

The LEMI-423 recordings are all time synchronised from the on-board GPS, to improve the data processing with remote referencing. The electrical field fluctuation, E*x* & E*y* (with *x* north and *y* east), for all sites were calculated by:

$$\Delta U = E \cdot d$$

Where, ΔU, the measured potential difference between a pair of electrodes at, d, distance apart that together form a dipole with a typical length of 50 m. The electrodes used were Cu-$CuSO_4$ non-polarising porous ceramic LEMI-701 electrodes orientated to magnetic north-south and east-west. The unit of measurement used for E was $\mu V/m$.

The magnetic induction components, B*x* and B*y* (with *x* north and *y* east), were recorded using LEMI-120 induction coil magnetometers that were orientated parallel to the electrical dipoles spaced 5 meters apart. The frequency range for the induction coils are of the order of 0.001 to 1000 Hz, with measurements calibrated in the frequency

domain to ρT. Each station was rotated to geographic coordinates using the geomagnetic declination of the area, which ranged from 7° - 8°.

Time windows were then selected for each site, with periods of high geomagnetic activity being more favourable. The data were sampled at 1000 Hz, but due to software limitations only several hours of data can be processed at this sampling rate. Thus, the data were also processed over a longer time window (48 hours) with a lower sampling rate of 10 Hz.

The raw time series data were Fourier transformed for each site to the frequency domain using the bounded influence remote-reference processing (BIRRP) method (Chave & Thomson, 2004). The aim of the process was to remove outliers in the time series measurements, produce a robust estimation of the transfer function, and obtain a series of power spectral estimates of the electric and magnetic fields.

Each processed data window was visually assessed on the quality of the apparent resistivity and phase plots, with noisy data windows reprocessed with different time windows for each station. The final selection of data windows for the 1000 Hz and 10 Hz data where then combined into a single EDI file to obtain the maximum frequency range of data.

In addition to the CCMT-17 data that was collected for this project, three additional data sets were used, to get a regional sense of the resistivity structure in the Curnamona Province. They are the AusLAMP, 08GA-C1 and data collected from the University of Adelaide in two surveys. The 08GA-C1 data was from Geoscience Australia's north-south 2008 seismic traverse, where 25 sites were spaced an average of 10 km apart, with five components (Bx, By, Ex, Ey, Bz) of broadband (Milligan & Lilley, 2010).

FIELD DATA

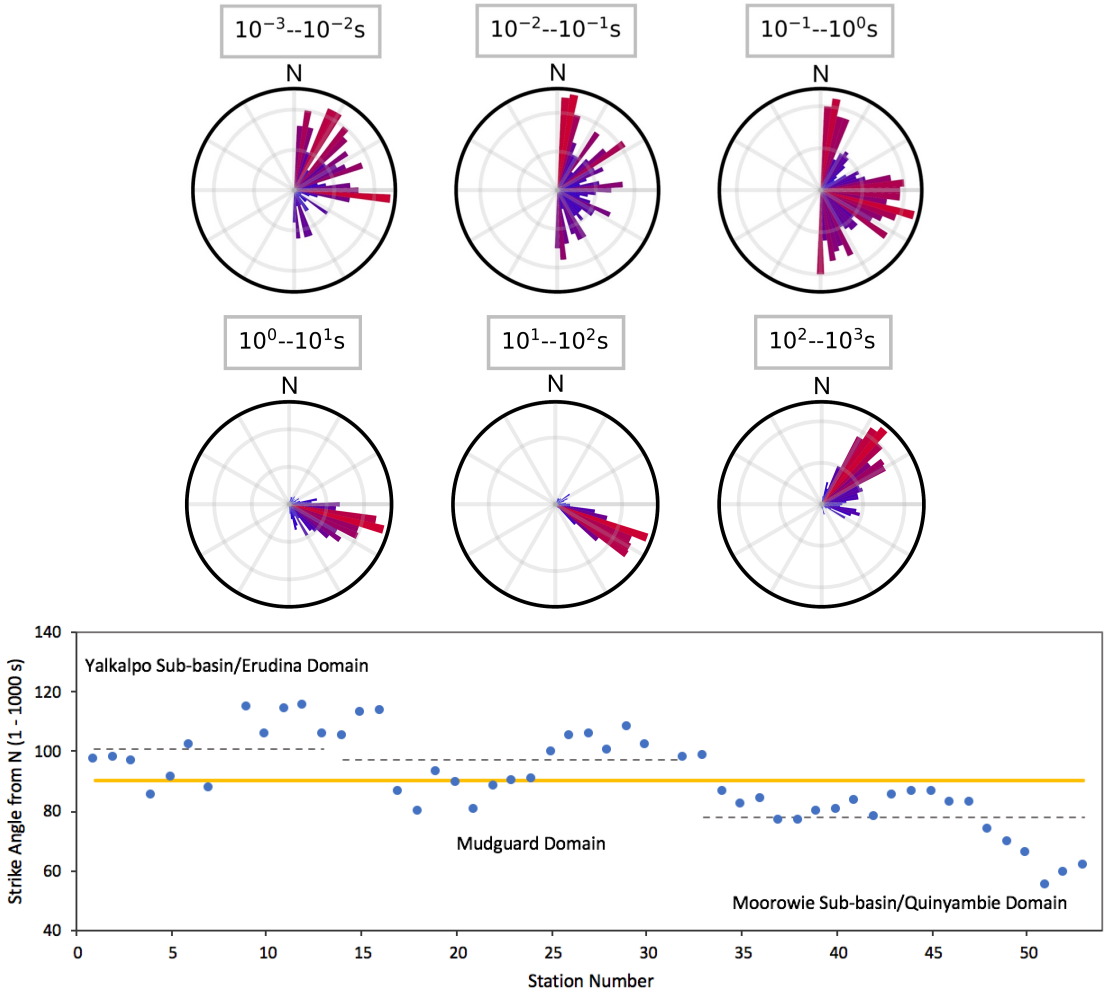

Figure 5: Geoelectric strike determination from the invariants of the impedance tensor (Weaver, Agarwal, & Lilley, 2000) for CCMT-17 transect. Top: Strike plotted as a rose plot in individual decades from MTpy (Krieger & Peacock, 2014). Bottom: Period averaged strike angle for each station with average strike of 90° (solid yellow line). Dashed lines show average strike directions for each geological domain.

The CCMT-17 transect shown in Figure 2 was chosen upon the 3D AusLAMP resistivity model of Robertson et al. (2016), on the premise that the structural elements were approximately 2D as shown in Figure 1. To demonstrate this, Figure 4 shows that this is indeed the case with strike analysis from the CCMT-17 transect returning an average geoelectric strike at 90° from north as shown in Figure 3b. Figure 3a shows how the geoelectric strike from the top sedimentary layer at decades 10^{-3} – 10^{0} s has a large variance with an approximately 1D structure (note, how there is a 90° strike

ambiguity between periods 10^2 – 10^3 and 10^0 – 10^2 s), thus only decades 10^0 – 10^3 s were used for the strike determination which show a 2D structure.

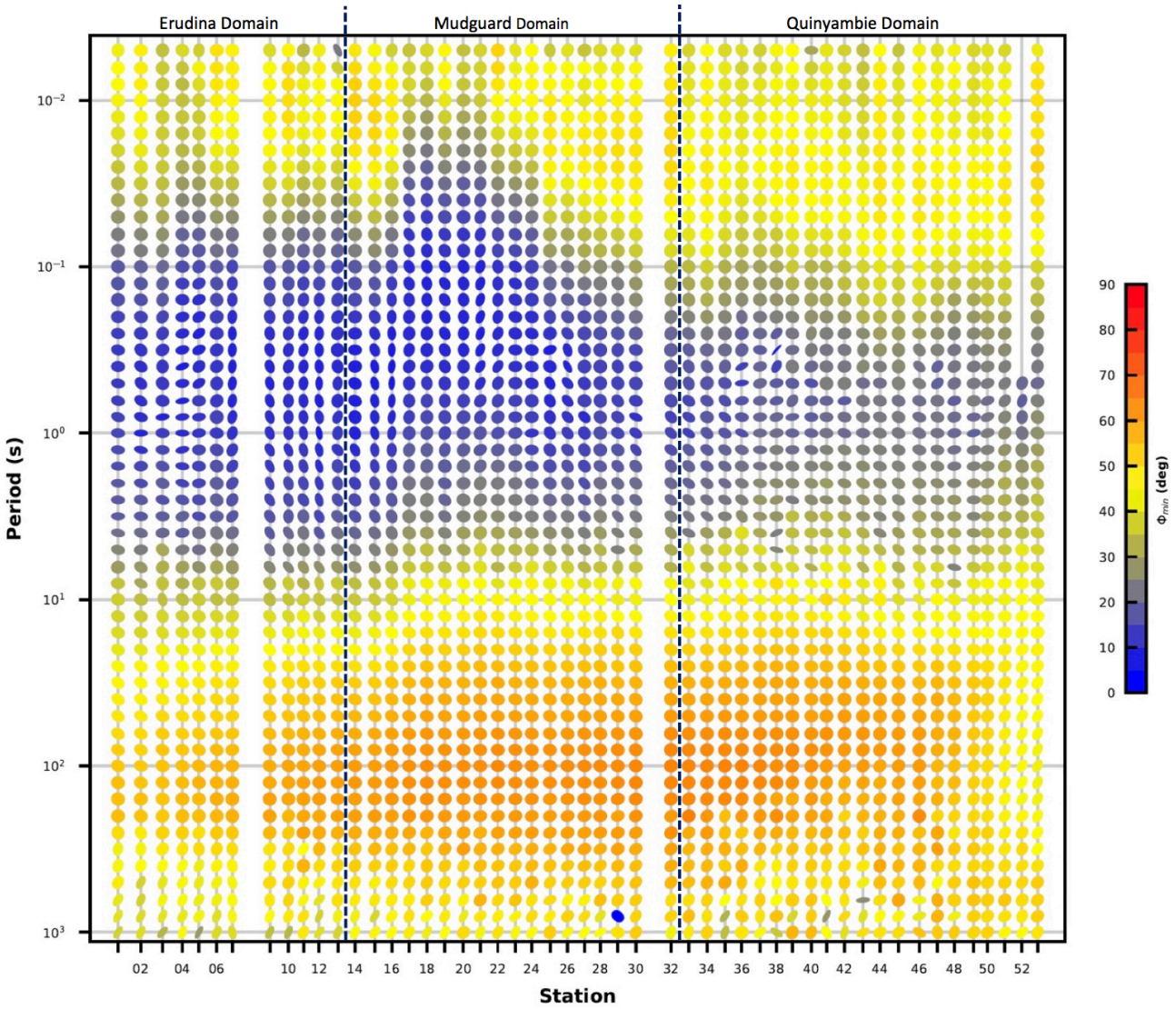

Figure 6: Phase tensor ellipse pseudosection for observed data, shaded by the minimum phase angle. Minimum phase angles; > 45° indicate structure becoming more conductive with depth; < 45° indicate structure becoming more resistive with depth. The distance between each station is 2 km. Geological domains are separated by the dashed black lines. Pseudosection was produced in MTpy (Krieger & Peacock, 2014).

The dimensionality from the phase tensor ellipses in Figure 5 for the CCMT-17 transect overall shows a very 1D structure, as shown by how circular the ellipses are, which clear regions delineated by the invariant minimum phase angle. With the top sedimentary layer, starting from 40^{-2} s, the average min phase is varying from 35° - 55° indicating a conductivity typical of sedimentary cover, with a zone of lower minimum

phase angle from stations 16 to 21 clearly seen in Figure 6 on the TMI image that is situated near a shear zone. There is a large increase in the resistivity from 10^{-1} s, as shown by the sharp change in the minimum phase angle to < 20°, that is more evident in the western half of the transect. From 10^{1} s, the conductivity increases as shown by the minimum phase angle of > 60°, before gradually losing resolution near 10^{3} s, as depicted by the changes in ellipse orientation and minimum phase angle. From the dimensionality analysis, it was decided to rotate the processed data prior to 2D modelling.

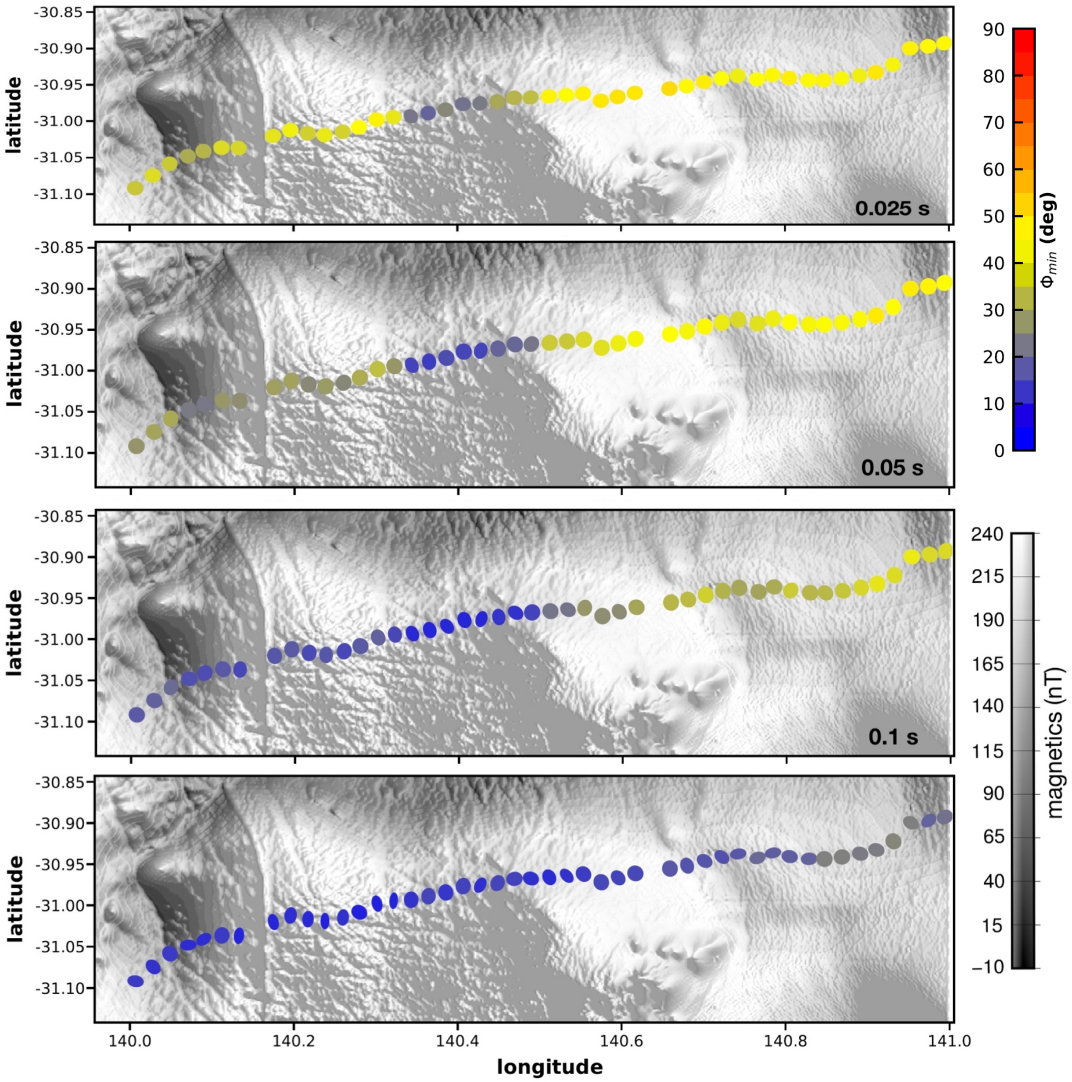

Figure 7: Phase tensor ellipses plotted at periods, from top to bottom, of 0.02 (50 Hz), 0.05 (20 Hz), 0.1 (10 Hz) and 1 (1Hz) s, overlaying greyscale RTP TMI. Phase tensor ellipses are shaded according to the phase minimum value.

Modelling

The processed data were rotated to strike ~10° east of north and the two modes are shown in Figure 8. The pseudosections in Figure 4 show the observed TE & TM modes as a function of period. The data for both modes are very smooth showing little heterogeneity and negligible effects from static-shift due to the conductive top layer. The resistivity for both modes identifies features close to the surface but struggles to identify further features at greater depths, while the phase for both modes is more able to identify deeper features, a common problem with the MT method is resolving features below conductors. Observed from $10^1 – 10^2$ s there is a general trend from west to east that indicates a conductive top layer with a resistive body underneath that eventually thins out as the subsurface becomes more conductive to the east.

A smooth model inversion using the algorithm of Rodi & Mackie (2001) was used for the 2D inversion. TE and TM modes were both used to model the data with decades from $10^{-3} – 10^3$ s. The smooth inversion is determined by the data misfit and the model constraint, which is defined by the regularisation parameter, tau. Where the higher the tau value the smoother the model is, the final model had a tau value of 1. As shown in Figure 2, the topography over the transect is negligible and due to computational limitations was not included in the modelling parameters. The resistivity and phase floor errors were set to 5% and 2.5%, respectively. The final RMS was 1.93 where a value of < 1 is considered an overfit, $>> 1$ an under fit and ~ 1 an ideal fit for the model if there was no noise.

The 2D inversion model reveals three resistive zones and three zones of high electrical conductivity beneath the CCMT-17 transect in the Curnamona Province (Figure 9, Top). The high conductivity material beneath the boundary at the Erudina

and Mudguard Domains is labelled as C1; beneath the Quinyambie Domain is labelled C2; beneath the Mudguard Domain is labelled C3 between the depths of 15 - ~25 km, ~5 - ~8 km and ~0.3 - ~10 km, respectively. The resistive zones beneath the Erudina Domain is labelled as R1; beneath the Mudguard Domain is labelled as R2; beneath the Quinyambie Domain is labelled R3.

A conductive top layer at 1 Ω m from the surface to approximately 200 m is present from along the profile, with a section from 40 – 55 km thinning to approximately 100 m. The largest conductive anomaly, C1, is widespread starting from a depth of 14 km and extending over 40 km long with readings of 1 Ω m. Another conductive anomaly, C2, is situated from 80 – 100 km along the profile at a depth of 4 km, with reading 5 Ω m. From 500 m to approximately 6 km there is a large near continuous resistive zone, R1, R2 and R3, at approximately 10,000 Ω m ranges across the whole profile length that's separated by two areas of higher conductivity. The last feature is the near vertical feature, C3, 45 km along the profile at a depth of 10 km to 400 m with a small offshoot near 2 km also going up towards the surface at 100 Ω m.

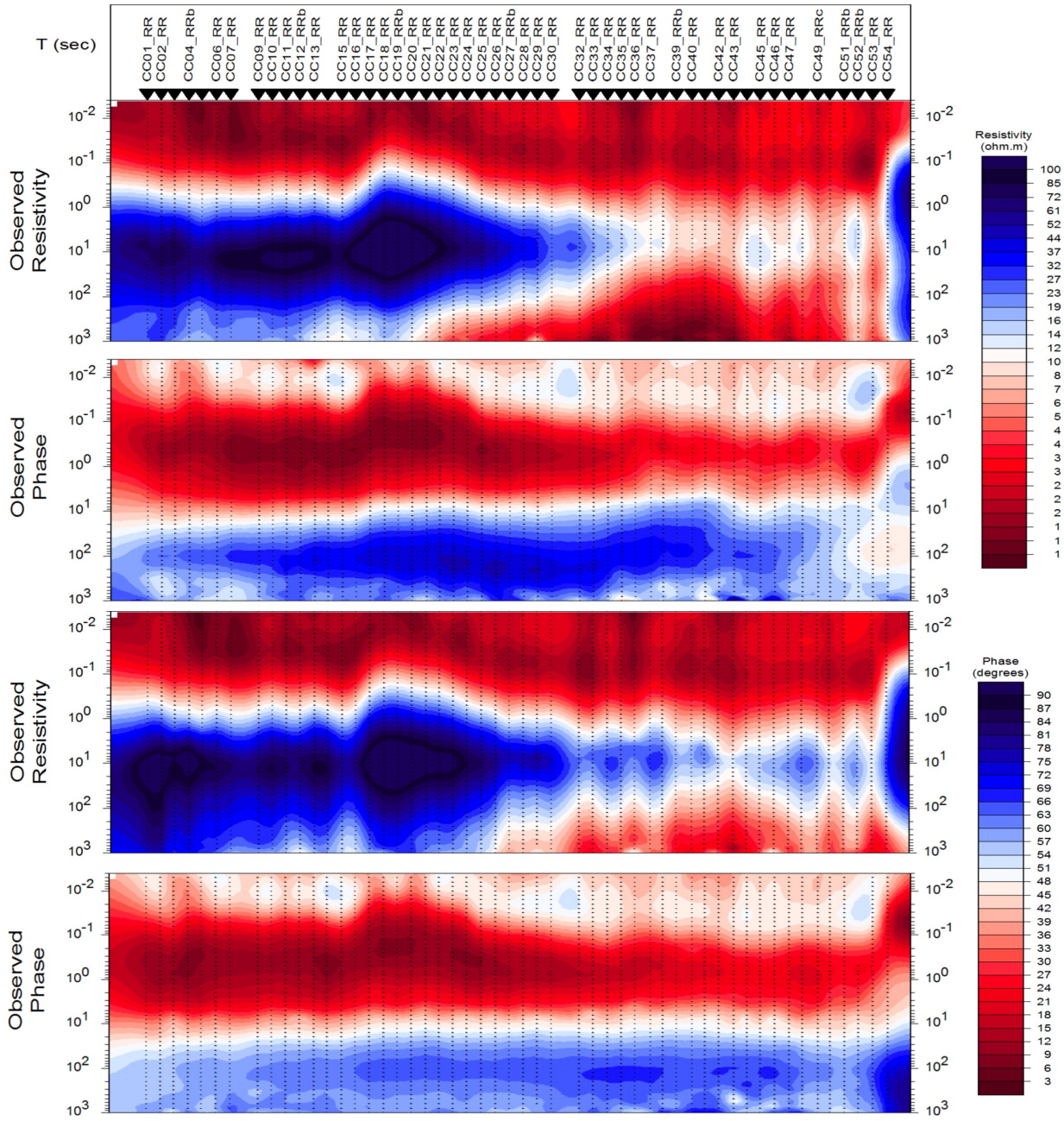

Figure 8: Pseudosections showing the TE and TM modes for the observed data from the 2D model as a function of period. Spacing between each station is 2 km.

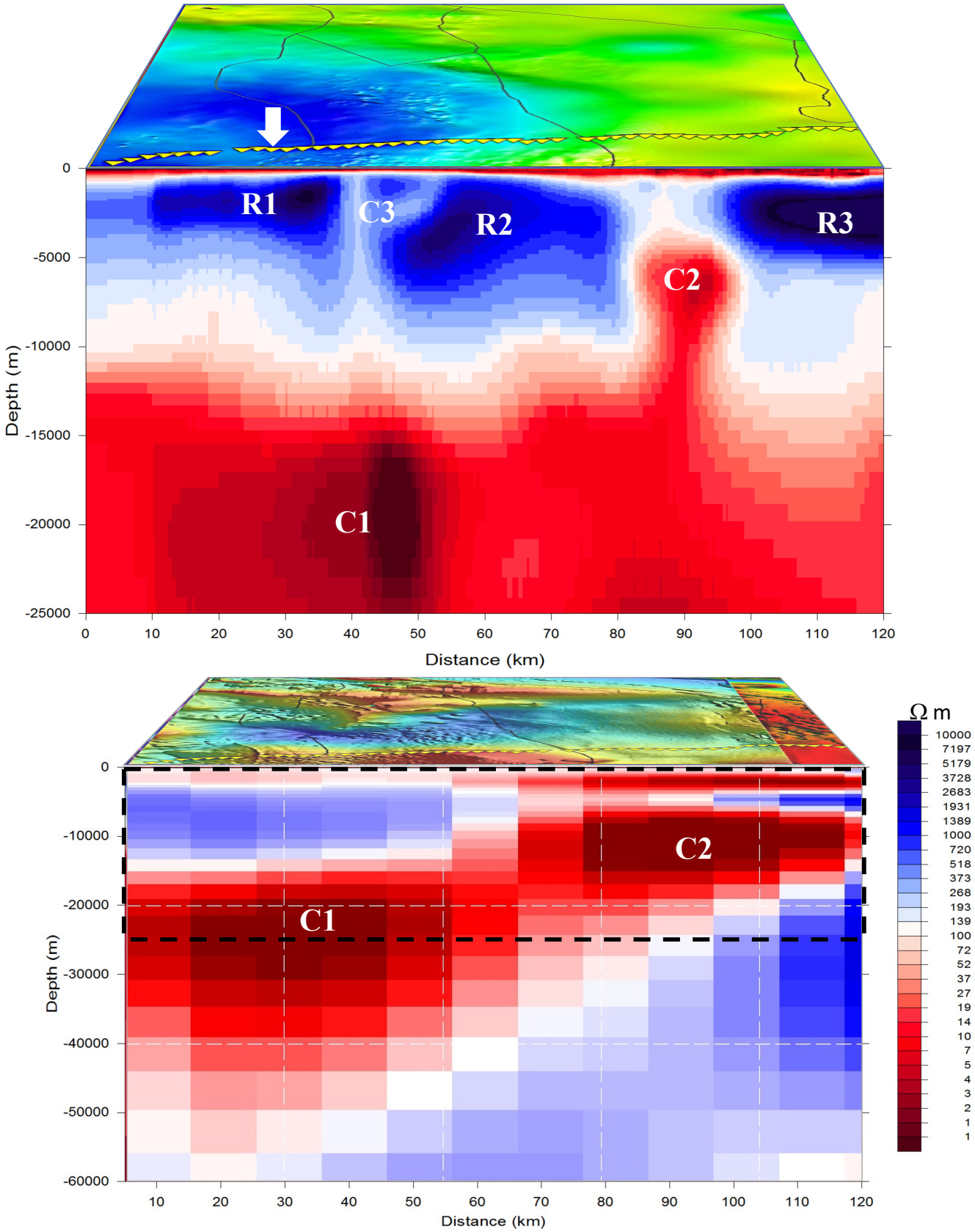

Figure 9: Top: Resistivity model obtained from 2D inversion of observed data from CCMT-17 transect with Bouguer Gravity image for perspective. Bottom: Resistivity cross section of AusLAMP data across CCMT-17 transect (Robinson et al., (2016)) with RTP TMI image for perspective. Black dashed line showing extent of the 2D resistivity model from CCMT-17. Yellow triangles show MT site locations for CCMT-17. White arrow points to site 11, the intersect point.

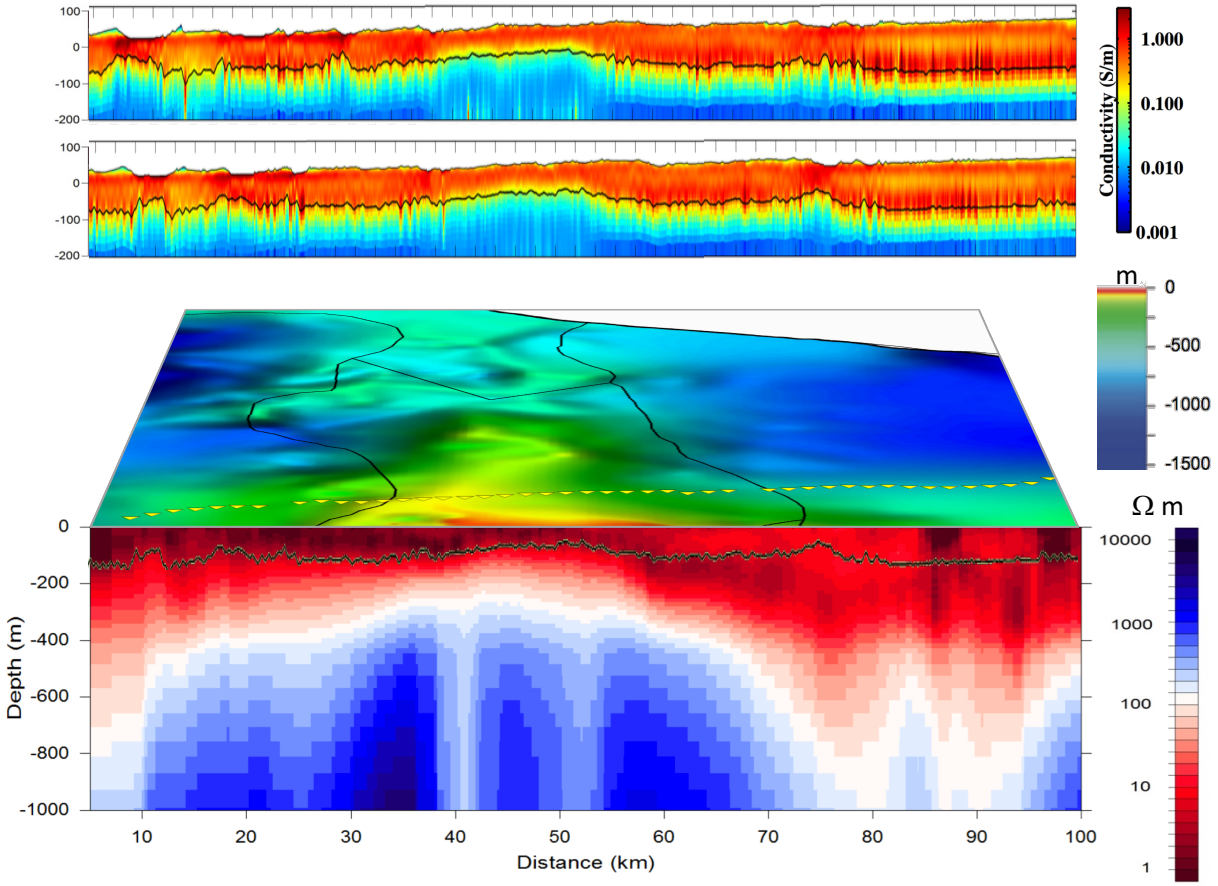

Figure 10: Top: Frome AEM survey line #2000101, located parallel of model profile ~1.2 km north, showing conductivity to 200 m depth. Middle: Frome AEM survey line #2000201, located parallel of model profile ~1.2 km south, showing conductivity to 200 m depth. Bottom: Resistivity model from 2D inversion of observed data with depth to 1000 m within South Australia, with depth to Proterozoic Basement added for perspective (Fabris, Gouthas, & Fairclough, 2010). Black line shows estimated depth to sediments from Frome AEM survey line # 2000201.

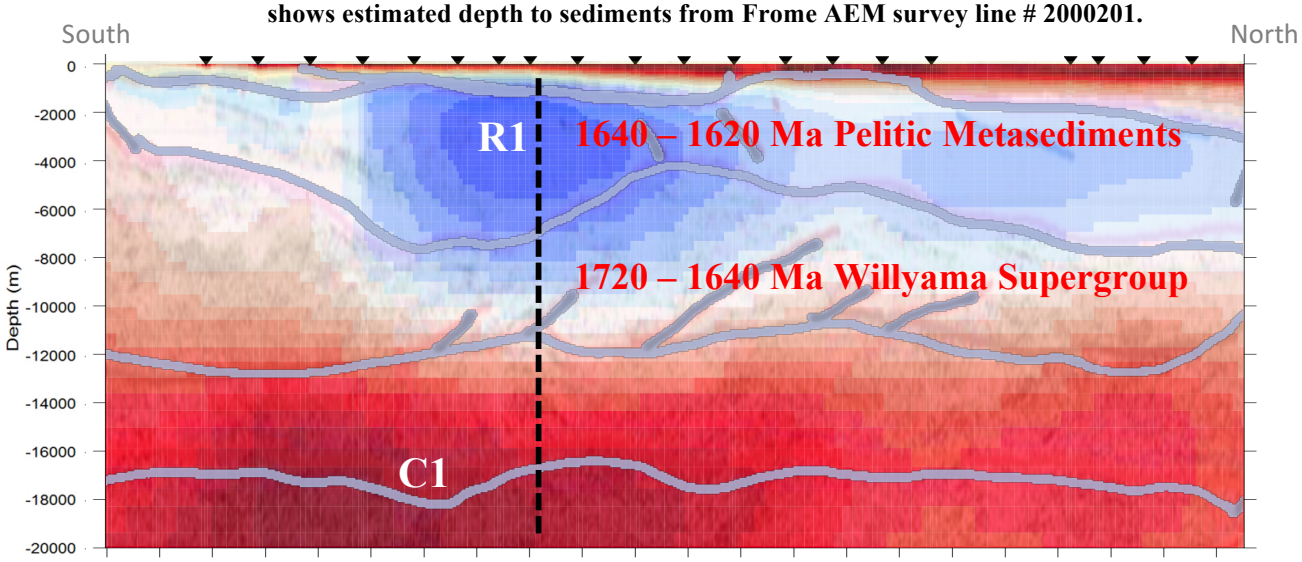

Figure 11: Resistivity model obtained from 2D inversion of observed data for transect 08GA-C1. Overlain is grey are the interpreted boundaries and faults from seismic reflections as interpreted from Korsch et al. (2010). Blue resistive zone interpreted to be 1640 – 1620 Ma pelitic metasedimentary rocks, white zone interpreted to be 1720 – 1640 Ma Willyama Supergroup and red conductive zone is unknown basement from Korsch et al. (2010). Black dashed line shows where the above model intersects with the CCMT-17 site 11.

DISCUSSION

When comparing the two different models, from Robertson et al. (2016) AusLAMP 3D model and the CCMT-17 2D inversion discussed in this paper, they show remarkable similarities for the starting depth of the two low resistivity zones, C1 and C2 (Figure 9). As shown in Figure 9, by reducing the scale of site sampling from approximately 50 km as used for the AusLAMP sites, by a factor of 25, to site spacing of 2 km used in the CCMT-17 transect, has delineated the features of the Curnamona Conductor to a higher resolution however due to the conductors absorbing the signal like a sponge the resolution at depth is lost.

One significant feature from the 2D resistivity inversion is C3 at 100 Ω m that has a footprint from the brittle-ductile boundary near 10 km (Thiel et al., 2016), above the C1 conductor, to the topographic basement high (Figure 10). A possible cause of this footprint is from fluids accumulating below the brittle-ductile boundary, until overpressure results in hydro-fracturing of the brittle crust above (Connolly & Podladchikov, 2004) resulting in a conductive footprint from the alteration of fossil fluid pathways, usually through zones of weakness, which have previously been observed at mineral deposit locations such as Olympic Dam (Heinson, Direen, & Gill, 2006). As seen in Figure 7, a possible zone of weakness are the unnamed faults easily seen from the greyscale total magnetic image.

The conductor, C2, is situated at the boundary near a major unnamed fault that is situated on the eastern edge of the benagerie ridge, that might have acted as a pathway for the conductive fluids. Though when using the OZ SEEBASE depth to Proterozoic basement the C2 conductor is situated at the base of the Moorowie sub-basin, which is interpreted to be 6 km deep where the conductivity might be from saline aqueous fluids

in porous sediments however Fabris et al. (2010) depth to basement model, which is further constrained through seismic and drill core data, has the Moorowie sub-basin depth from 1 – 2 km which will eliminate saline fluids as the conductor mechanism. It is possible to speculate that the large C2 conductor, with a width of approximately 15 km and possible length > 80 km (Figure 1), might have had a large scale thermal effect that has weakened the crustal rheology (Corti et al., 2003) that when compounded with paleo-stresses lead to the eventual formation of the Moorowie sub-basin during the Cambrian.

Though the two traverses, 08GA-C1 and CCMT-17, were unconstrained from each other they show remarkable similarities in the MT response. Thus, from stacking the 08GA-C1 seismic traverse from Korsch et al. (2010) together with the 2D resistivity model has enabled a tentative interpretation for the CCMT-17 2D model based on where the profiles intercept (Figure 11). From this we can speculate that zones R1 and R2 are part of the non-reflective 1640 – 1620 Ma pelitic metasedimentary blanket, though depending on how laterally extensive it is, R3 might tentatively be included as well. The zones where the resistivity decreases to approximately 100 Ω m near depths of 10 km, was interpreted by Korsch et al. (2010) as belonging to the 1720 – 1640 Ma Willyama Supergroup (Figure 11). The C1 conductor, though having a good reflective return from the seismic traverse, is unknown at depth due to no outcrop or xenolith data that corresponds to it.

Figure 10, a slice of the top 1000 m from the 2D resistivity model, shows the conductivity of the sedimentary cover. There is a strong correlation between the AEM Frome survey data and the closely spaced BB MT data in delineating the sediment cover for the top 150 m, before the AEM depth of penetration decreases as the

sedimentary cover increase near the Moorowie sub-basin. The dark red in figure 10, at 1 Ω m, shows a uniform conductive layer above the basement rock, when you compare this to sea water with a conductivity of 1/3rd Ω m, you can understand why the AEM struggled to penetrate to greater depths. The depth to basement can be considered within the range of 100 Ω m to 50 Ω m, this compares favourably with the depth to basement model of Fabris et al., (2010).

CONCLUSIONS

Through scale-reduction of AusLAMP, 50 km spaced long period data, to broadband MT, with 2 km site spacing, has greatly improved the understanding of previously unknown connections between the mid to lower crustal Curnamona Conductor and the surface. This increase in resolution and bandwidth, that has resulted in the identification of unknown fluid pathways from the mid upper crust to the near surface has shown that it's possible through scale reduction to increase confidence in exploration undercover, especially in greenfield areas by approaching it from a mineral systems framework, that being from the whole of lithosphere to the near surface.

ACKNOWLEDGMENTS

I'd like to thank my supervisor Graham Heinson for all his support this year. This project would not have been possible without the Geological Survey of South Australia (GSSA) by providing PACE Copper funding for the SA sites, and ASEG Research Foundation for providing funding for the NSW sites. Logistical support was provided by Havilah Resources by accommodating the field crew at the Portia Mine Site in South Australia. Goran Boran for your technical support and showing how to deploy the MT instruments out in the field. Yohannes Didana for your explanations into

the MT modelling process and field work assistance. Kate Robinson for your work done on the Curnamona Conductor through AusLAMP and your help in the draft thesis. GSSA AuScope for providing the BB MT instruments. Figures were produced from GMT and MTPy.

REFERENCES

CAGNIARD, L. (1953). Basic Theory of the Magneto-Telluric Method. *Geophysics*, *18*, 605–635.

CALDWELL, T. G., BIBBY, H. M., & BROWN, C. (2004). The magnetotelluric phase tensor. *Geophysical Journal International*, *158*, 457–469. HTTPS://DOI.ORG/10.1111/J.1365-246X.2004.02281.X

CHAVE, A., & JONES, A. (2012). *The Magnetotelluric Method*. Cambridge University Press.

CHAVE, A., & THOMSON, D. (2004). Bounded influence magnetotelluric response function estimation. *Geophysical Journal International*, *157*.

CONNOLLY, J. A. D., & PODLADCHIKOV, Y. (2004). Fluid flow in compressive tectonic settings : Implications for midcrustal seismic reflectors and downward fluid migration. *Journal of Geophysical Research*, *109*, 1–12. HTTPS://DOI.ORG/10.1029/2003JB002822

CONOR, C. H. H., & PREISS, W. V. (2008). Understanding the 1720 – 1640 Ma Palaeoproterozoic Willyama Supergroup , Curnamona Province , Southeastern Australia : Implications for tectonics , basin evolution and ore genesis, *166*, 297–317. HTTPS://DOI.ORG/10.1016/J.PRECAMRES.2007.08.020

CORTI, G., BONINI, M., CONTICELLI, S., INNOCENTI, F., MANETTI, P., SOKOUTIS, D., … PIRA, G. LA. (2003). Analogue modelling of continental extension : a review focused on the relations between the patterns of deformation and the presence of magma. *Earth-Science Reviews*, *63*, 169–247. HTTPS://DOI.ORG/10.1016/S0012-8252(03)00035-7

FABRIS, A., GOUTHAS, G., & FAIRCLOUGH, M. (2010). The new 3D sedimentary basin model of the Curnamona Province : geological overview and exploration implications The new 3D sedimentary basin model of the Curnamona Province : geological overview and exploration implications. *MESA Journal*, *58*(September 2010), 16–24.

FRICKE, C. E., PREISS, W. V, & NEUMANN, N. L. (2010). Curnamona Province : a Paleo- to Mesoproterozoic time slice. *In: Korsch, R.J. and Kositcin, N., Editors, South Australian Seismic and MT Workshop 2010. Geoscience Australia, Record, 2010/10,* 22–33.

GAMBLE, T., GOUBAU, W., & CLARKE, J. (1979). Error analysis for remote reference magnetotellurics. *Geophysics*, *44*(5), 959–968.

HEINSON, G. S., DIREEN, N. G., & GILL, R. M. (2006). Magnetotelluric evidence for a deep-crustal mineralizing system beneath the Olympic Dam iron oxide copper-gold deposit , southern Australia. *Geology*, (7), 573–576. HTTPS://DOI.ORG/10.1130/G22222.1

JONES, A. G. (1988). SfaUc shiff of magnetotelluric data and its removal in a sedimentary basin environment, *53*(7), 967–978.

KOSITCIN, N. (2010). *Geodynamic Synthesis of the Gawler Craton and Curnamona Province Geodynamic Synthesis of the Gawler Craton and Curnamona Province*.

KRIEGER, L., & PEACOCK, J. R. (2014). MTpy: A Python toolbox for magnetotellurics. *Computers and Geosciences*, *72*, 167–175. HTTPS://DOI.ORG/10.1016/J.CAGEO.2014.07.013

MCCUAIG, C., & HRONSKY, J. (2014). The mineral system concept : The key to exploration targeting. *Society of Economic Geologists Special Publication*, *18*(2014), 153–175. HTTPS://DOI.ORG/10.1080/03717453.2017.1306274

MILLIGAN, P. R., & LILLEY, F. (2010). Magnetotelluric results along the N-S Curnamona seismic traverse to the east of Lake Frome , South Australia. *ASEG Extended Abstracts*, 1–4.

PAGE, R., & LAING, W. (1992). Felsic Metavolcanic Rocks Related to the Broken Hill Pb-Zn-Ag Orebody , Australia : Geology , Depositional Age , and Timing of High-Grade Metamorphism. *Economic Geology*, *87*(1988), 2138–2168.

PREISS, W. V. (2000). The Adelaide Geosyncline of South Australia and its significance in Neoproterozoic continental reconstruction. *Precambrian Research*, *100*, 21–63.

PREISS, W. V, FOMIN, T., GOLEBY, B. R., KORSCH, R. J., ROBERTSON, R. S., BURTT, A. C., … RANGES, F. (2004). THE ADELAIDEAN AND CAMBRIAN COVER SUCCESSION OF THE CURNAMONA PROVINCE.

ROACH, I. (2012). *The Frome airborne electromagnetic survey , South Australia : Implications for energy, minerals and regional geology*.

ROACH, I. C., JAIRETH, S., & COSTELLOE, M. T. (2014). Applying regional airborne electromagnetic (AEM) surveying to understand the architecture of sandstone-hosted uranium mineral systems in the Callabonna Sub-basin , Lake Frome region , South Australia Applying regional airborne electromagnetic (AEM) surveying to understand the architecture of sandstone-. *Australian Journal of Earth Sciences*, *61*(5), 659–688. HTTPS://DOI.ORG/10.1080/08120099.2014.908951

ROBERTSON, K., HEINSON, G., & THIEL, S. (2016). Lithospheric reworking at the Proterozoic – Phanerozoic transition of Australia imaged using AusLAMP Magnetotelluric data. *Earth and Planetary Science Letters*, *452*, 27–35. HTTPS://DOI.ORG/10.1016/J.EPSL.2016.07.036

ROBERTSON, R., PREISS, W., CROOKS, A., HILL, P., & SHEARD, M. (1998). Review of the Proterozoic geology and mineral potential of the Curnamona Province in South Australia. *AGSO Journal of Australian Geology & Geophysics*, *17*(3), 169–182.

RODI, W., & MACKIE, R. L. (2001). Nonlinear conjugate gradients algorithm for 2-D magnetotelluric inversion. *Geophysics*, *66*(1), 174–187.

SIMPSON, F., & BAHR, K. (2005). *Practical Magnetotellurics*. Cambridge University Press.

THIEL, S., SOEFFKY, P., KRIEGER, L., PEACOCK, J., & HEINSON, G. (2016). Conductivity response to intraplate deformation: Evidence for metamorphic devolatilization and crustal-scale fluid focusing. *Geophysical Research Letters*, 1–9. HTTPS://DOI.ORG/10.1002/2016GL071351.ABSTRACT

TIKHONOV, A. N. (1950). On Determining Electrical Characteristics of the Deep Layers of the Earth's Crust. *Doklady*, *2*, 295–297.

WEAVER, J. T., AGARWAL, A. K., & LILLEY, F. E. M. (2000). Characterization of the magnetotelluric tensor in terms of its invariants. *Geophysical Journal*

International, *141*, 321–336.

APPENDIX A: SITE STATION INFORMATION

SiteName	Date & Time	Lat	Long	Elevation
CC_RR	06/07/17 10:51:11	-31.45922	140.54476	
CC_01	06/07/17 15:15:18	-31.09779	140.01786	24
CC_02	06/07/17 15:30:01	-31.07456	140.02846	24
CC_03	06/07/17 16:23:54	-31.06287	140.04534	15
CC_04	06/07/17 16:42:41	-31.048	140.0711	15
CC_05	07/07/17 09:53:58	-31.04104	140.09016	21
CC_06	07/07/17 10:20:54	-31.03638	140.11227	35
CC_07	07/07/17 10:47:28	-31.03674	140.13316	21
CC_09	07/07/17 11:32:28	-31.02016	140.17522	32
CC_10	07/07/17 12:09:51	-31.01218	140.192	33
CC_11	07/07/17 12:25:54	-31.01662	140.21744	26
CC_12	07/07/17 12:56:23	-31.01897	140.23804	35
CC_13	08/07/17 11:32:37	-31.0146	140.26013	29
CC_14	08/07/17 12:06:29	-31.00892	140.27992	39
CC_15	08/07/17 12:39:55	-30.99785	140.30153	45
CC_16	08/07/17 13:14:48	-30.99429	140.32205	34
CC_17	09/07/17 12:15:43	-30.9932	140.34316	28.7
CC_18	10/07/17 11:01:12	-30.988783	140.364546	26.2
CC_19	09/07/17 12:58:28	-30.98426	140.38562	43
CC_20	09/07/17 13:39:47	-30.97659	140.40683	48
CC_21	09/07/17 11:59:58	-30.97546	140.4276	51
CC_22	09/07/17 12:45:11	-30.97297	140.44876	52
CC_23	09/07/17 13:31:38	-30.96782	140.46935	63
CC_24	09/07/17 14:24:36	-30.96734	140.48946	3
CC_25	10/07/17 12:25:53	-30.96582	140.51183	64
CC_26	10/07/17 13:07:17	-30.969401	140.53314	65
CC_27	10/07/17 13:47:07	-30.96196	140.55359	51
CC_28	10/07/17 14:32:21	-30.97185	140.57523	45
CC_29	11/07/17 11:46:31	-30.97118	140.59565	51.5
CC_30	11/07/17 12:22:04	-30.96111	140.61682	55
CC_31	01/01/70 09:30:00	-30.95716	140.63803	57

SiteName	Date & Time	Lat	Long	Elevation
CC_32	11/07/17 13:37:28	-30.95528	140.65889	61
CC_33	11/07/17 11:50:17	-30.95178	140.6799	59
CC_34	11/07/17 12:37:17	-30.94603	140.70122	63
CC_35	11/07/17 13:21:54	-30.94119	140.72227	62
CC_36	11/07/17 14:01:11	-30.93746	140.74228	51
CC_37	12/07/17 11:16:28	-30.94178	140.76523	52.8
CC_38	12/07/17 11:49:41	-30.93491	140.78368	55.1
CC_39	12/07/17 12:17:05	-30.94016	140.80421	58.4
CC_40	12/07/17 12:54:52	-30.94336	140.82838	54.1
CC_41	13/07/17 10:53:39	-30.943617	140.84735	52.9
CC_42	13/07/17 11:27:40	-30.94114	140.8688	56
CC_43	13/07/17 11:52:53	-30.93717	140.89095	55
CC_44	13/07/17 12:29:51	-30.93262	140.91072	59
CC_45	13/07/17 13:06:19	-30.922189	140.93151	59.8
CC_46	13/07/17 13:44:08	-30.89975	140.952781	69.4
CC_47	13/07/17 14:24:44	-30.89701	140.97459	69
CC_48	13/07/17 15:00:51	-30.892817	140.994255	66
CC_49	25/07/17 11:35:13	-30.8917	141.01808	70.2
CC_50	25/07/17 13:00:16	-30.895733	141.03559	74.8
CC_51	25/07/17 12:41:58	-30.899917	141.057686	73.6
CC_52	25/07/17 14:15:59	-30.897033	141.078217	73.1
CC_53	25/07/17 13:50:12	-30.916267	141.100495	79.9
CC_54	25/07/17 14:47:34	-30.9258	141.122364	82.8
CC_56	25/07/17 15:22:10	-30.927733	141.165069	86
CC_58	25/07/17 15:49:01	-30.937033	141.204772	93.3
CC_60	25/07/17 16:43:15	-30.935517	141.24925	105.3
CC_62	25/07/17 16:45:54	-30.905133	141.290462	106